Direct Light Orbital Angular Momentum Detection in Mid-Infrared Based on the Type-II Weyl Semimetal TaIrTe$_4$

Jiawei Lai, Junchao Ma, Zipu Fan, Xiaoming Song, Peng Yu, Zheng Liu, Pei Zhang, Yi Shi, Jinluo Cheng, and Dong Sun*

The direct photocurrent detection capability of light orbital angular momentum (OAM) has recently been realized with topological Weyl semimetals, but it is limited to the near-infrared wavelength range. The extension of the direct OAM detection capability to the mid-infrared band, which is a wave band that plays an important role in a vast range of applications, has not yet been realized. This is because the photocurrent responses of most photodetectors are neither sensitive to the phase information nor efficient in the mid-infrared region. In this study, a photodetector based on the type-II Weyl semimetal tantalum iridium telluride (TaIrTe$_4$) is designed with peculiar electrode geometries to directly detect the topological charge of the OAM using the orbital photogalvanic effect (OPGE). The results indicate that the helical phase gradient of light can be distinguished by a current winding around the optical beam axis, with a magnitude proportional to its quantized OAM mode number. The topologically enhanced responses in the mid-infrared region of TaIrTe$_4$ further help overcome the low responsivity issues and finally render direct OAM detection capability. This study enables on-chip-integrated OAM detection, and thus OAM-sensitive focal plane arrays in the mid-infrared region.

1. Introduction

Since the introduction of optical vortices in 1989, many break-throughs have been achieved for their applications in various fields,[1] including optical manipulation,[2] machining,[3] imaging,[4] quantum optics,[5] optical and quantum communications,[6] and even astrophysics.[7] The tremendous progress has benefited from rapid developments in the generation and manipulation of the orbital angular momentum (OAM) of light.[8] In particular, recent rapid progress in miniaturizing vortex generation and manipulation devices using on-chip micro- or nanoscale structures has boosted their on-chip integration for applications in optical sensing, micromanipulation, and optical communications in both the classical and quantum domains.[9] However, at the detection end, the techniques for measuring OAM are usually realized by adopting interference and diffraction properties, which require the indirect counting of the stripes and lattices in the interference or diffraction patterns, or carrying out indirect phase transformation.[10] The direct electric readout of OAM is highly desired, especially for system-level integrated applications that require on-chip integration and focal plane array imaging with OAM sensitivity.

Recent developments in the direct characterization of the topological charge of OAM based on the type-II Weyl semimetal tungsten ditelluride (WTe$_2$) have led to the direct electric

J. Lai, J. Ma, Z. Fan, D. Sun
International Center for Quantum Materials
School of Physics
Peking University
Beijing 100871, China
E-mail: sundong@pku.edu.cn

X. Song
State Key Laboratory of Precision Measurement Technology and Instruments
School of Precision Instruments and Opto-electronics Engineering
Tianjin University
Tianjin 300072, China

P. Yu
State Key Laboratory of Optoelectronic Materials and Technologies
Guangzhou Key Laboratory of Flexible Electronic Materials and Wearable Devices
School of Materials Science and Engineering
Sun Yat-sen University
Guangzhou, Guangdong 510275, China

Z. Liu
Centre for Programmed Materials
School of Materials Science and Engineering
Nanyang Technological University
Singapore 639798, Singapore

P. Zhang
Shaanxi Province Key Laboratory of Quantum Information and Quantum Optoelectronic Devices
School of Physics
Xi'an Jiaotong University
Xi'an 710049, China

Y. Shi
School of Electronic Science and Engineering
Nanjing University
Nanjing 210008, China

J. Cheng
Changchun Institute of Optics
Fine Mechanics and Physics
Chinese Academy of Sciences
Changchun 130033, China

D. Sun
Collaborative Innovation Center of Quantum Matter
Beijing 100871, China

**ADVANCED
SCIENCE NEWS**

www.advancedsciencenews.com

**ADVANCED
MATERIALS**

www.advmat.de

readout of OAM and subsequent on-chip integration.[11] Detection is achieved at a near-infrared wavelength (≈ 1 μm) based on the orbital photogalvanic effect (OPGE) driven by the helical phase gradient of light. The OAM mode number can be determined by the quantized magnitude of the current winding around the optical beam axis. However, there remain technical challenges with respect to extending direct OAM detection to mid-infrared wavelengths, which is highly desired for a vast range of OAM-related applications. Such a demand is especially urgent for mid-infrared focal plane array imaging, which is crucial for autonomous driving, night vision, and motion detection. There are two major technical obstacles in direct mid-infrared OAM detection. First, the light matter interaction is proportional to the variation of the vector potential associated with the OAM of light ($\approx 1/\lambda$); thus, the mid-infrared provides weaker interaction and thus a weaker influence on microscopic processes in materials compared to the near-infrared.[12] Second, the absolute photocurrent response is usually poor in the mid-infrared region, especially at room temperature. It cannot support a sufficient signal-to-noise ratio to distinguish the quantized magnitude associated with the OAM order despite the fact that such quantization is allowed by the symmetry of the detection material.

Recent developments in photodetection based on topological semimetals enabled the above issues to be addressed.[13] The photocurrent response can be boosted by the large Berry curvature near the Weyl nodes of a Weyl semimetal. When the doping level matches the optical transition wavelength, the topologically enhanced shift current response of a Weyl semimetal provides an efficient approach for obtaining high responsivity in the mid-infrared region.[13a,14] Some Weyl semimetals, such as tantalum iridium tellurides (TaIrTe$_4$), share the same crystal symmetry as WTe$_2$,[15] which allows quantized OPGE as a function of the OAM order. When combined with topologically enhanced responsivity, it potentially provides direct OAM detection capability in the mid-infrared region. In this work, we show that a photodetector based on the Type-II Weyl semimetal TaIrTe$_4$ with designed electrode geometries can achieve the direct detection of the topological charge of OAM through OPGE at 4 μm, which is a typical mid-infrared wavelength that is widely used for various applications. The observed OPGE response emerges from the phase gradient of the optical fields, rather than other photocurrent generation mechanisms, and the photocurrent driven by the OPGE is proportional to the OAM order of the incident beam. The beam size and spatial dependence measurements confirmed the efficient collection of the OPGE current as long as the spot size and position of the laser beam matched the electrode structure. Combined with the linear and circular polarization sensitivity demonstrated in a previous work,[13a,d] together with the conventional intensity sensitivity, a further carefully designed photodetector array device may be capable of full optical parameter characterization in the mid-infrared region.

2. OAM Detection and OPGE in TaIrTe$_4$

First, we analyzed the response of TaIrTe$_4$ under the illumination with OAM. In cylindrical coordinates, the OAM beams

with Laguerre–Gaussian (LG) modes propagating in the z direction are generally given by

$$\vec{\mathbf{E}}_{p,m}(r,\phi,z,t) = u_{p,|m|}(r,z)e^{im\phi}e^{i(k_z z - \omega t)}\hat{\varepsilon} + c.c.. \tag{1}$$

Here, $u_{p,|m|}(r,z)$ is the LG beam profile with the exact form given in Note S1, Supporting Information, $\vec{k} = k_z \hat{z}$ is the wave vector, ω is the light frequency, m is the OAM order, p is the radial quantum number, $\hat{\varepsilon} = \hat{\mathbf{x}} + i\sigma\hat{\mathbf{y}}$ represents the polarization of the beam, with $-1 \leq \sigma \leq 1$ being the optical helicity or spin angular momentum (SAM) of the beam ($\sigma = \pm 1$ for circular polarization), and $c.c.$ is the complex conjugate. When $m \neq 0$, a phase singularity appears at the center of the beam with zero light intensity; thus, the intensity profile appears as a ring. The radial quantum number p affects the radial electric field distribution of the LG beam. An intuitive manifestation of p relates to the number of rings in the intensity profiles (the number of rings equals to $p + 1$). In this study, only LG beams with $p = 0$ were considered. The beam radius at plane z is defined as $\sqrt{\frac{|m|}{2}}w(z)$ for the OAM order m, where $w(z)$ is the radius of the basic Gaussian beam at plane z when the spiral phase plates (SPPs) used to generate the OAM beam are removed. Note that this beam radius definition is different from the conventional one, but is more straightforward for practical measurements.[16]

The generation mechanisms of OPGE in materials belonging to the C_{2v} point group are described in detail in Ref. [11], using WTe$_2$ as an example. **Figure 1**a shows the crystalline structure of TaIrTe$_4$, which belongs to the point group C_{2v}. The OPGE response of TaIrTe$_4$ should qualitatively behave the same as WTe$_2$ from crystal symmetry considerations.[11] The nonlinear photocurrent response to the OAM of light arises from the gradient of the laser fields with the inclusion of the electric quadrupole and magnetic dipole effects. After a symmetry consideration is given in detail in Note S2, Supporting Information, the second-order direct current (DC) density generated from the OAM of light can be categorized into four terms according to their dependence on the experimentally tunable parameters SAM (σ) and OAM (m) as follows:

$$j^{(dc)}(r,\phi,z) = m \cdot \sigma j^{(1)}_{|m|}(r,\phi,z) + m j^{(2)}_{|m|,|\sigma|}(r,\phi,z) + \sigma j^{(3)}_{|m|}(r,\phi,z) + j^{(4)}_{|m|,|\sigma|}(r,\phi,z) \tag{2}$$

As an example, the distribution of $j^{(1)}_{|m|}$ in TaIrTe$_4$ can be described by two independent parameters β_1 and β_3, which are linear combinations of the non-vanishing planar rank-4 tensor β_{ijkl}, as defined by Equations (S6–S9) in Note S2, Supporting Information. $j^{(1)}_{|m|}$ can be written as:

$$j^{(1)}_{|m|}(r,\phi,z) = [\hat{\mathbf{r}}(\text{Im}[\beta_1] + \text{Im}[\beta_3]\cos 2\phi) + \hat{\phi}\text{Im}[\beta_3]\sin 2\phi] \frac{|u_{p,|m|}(r,z)|^2}{r} \tag{3}$$

where $\hat{\mathbf{r}}$ and $\hat{\phi}$ are the unit vectors along the radial and azimuthal directions, respectively. The specific expressions for $\mathbf{j}^{(2,3,4)}$ are given in Equations (S3–S5) in Note S2, Supporting Information. Note that the electric profile term ($u_{p,|m|}(r,z)$) of $j^{(1)}_{|m|}(r,\phi,z)$ depends on $|m|$. However, the measured current value is not the spatial distribution of the current density $j^{(1)}_{|m|}(r,\phi,z)$ itself, but is an integration of the current density over a certain region along either the radial or azimuthal directions, depending on the specific current collection geometry.
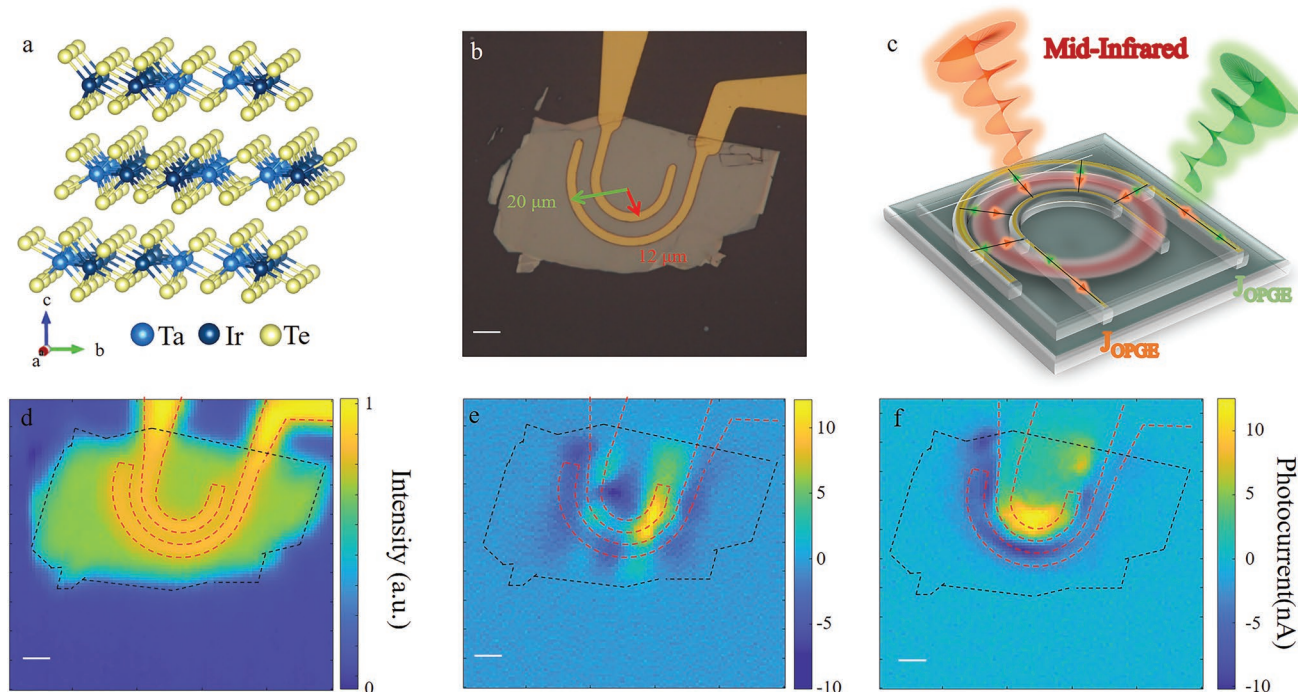
Figure 1. Basic characterization of the TaIrTe$_4$ sample. a) Crystal structures of TaIrTe$_4$ in the T_d phase. b) Optical image of a TaIrTe$_4$ device with U-shaped electrodes. c) Schematic of the OPGE response from light carrying opposite OAM orders. d) Scanning reflection image and e,f) photocurrent microscopy images of a TaIrTe$_4$ device with U-shaped electrodes at room temperature with 633 nm (e) and 4 µm (f) excitation, respectively. Each data point was measured in a single scan by a lock-in amplifier with a time constant of 30 ms. All scale bars are 10 µm.

In Note S3, Supporting Information, we further show that the integrated photocurrent response is approximately proportional to the beam energy, which is kept the same for different OAM orders in the measurement. Therefore, we denote the integrations of the terms $j_{|m|}^{(1)}$, $j_{|m|,|\sigma|}^{(2)}$, $j_{|m|}^{(3)}$, and $j_{|m|,|\sigma|}^{(4)}$ over the experimental geometry as capital letters $J^{(1)}$, $J_{|\sigma|}^{(2)}$, $J^{(3)}$, and $J_{|\sigma|}^{(4)}$, which do not depend on m or the sign of σ. Therefore, the four terms on the right-hand side of Equation (2) yields the measured current value $m \cdot \sigma J^{(1)} + m J_{|\sigma|}^{(2)} + \sigma J^{(3)} + J_{|\sigma|}^{(4)}$. We discuss how these terms contribute to different mechanisms. The OPGE responses arise from the helical phase gradient in the azimuthal direction, and they are determined by $m \cdot \sigma J^{(1)} + m J_{|\sigma|}^{(2)}$, which are proportional to the OAM order m; the circular photogalvanic effect (CPGE) gives nonzero photocurrents that are proportional to the SAM (σ), and it is determined by the term $m \cdot \sigma J^{(1)} + \sigma J^{(3)}$; for linear polarized OAM light ($\sigma \to 0$), the photocurrents are determined by the term $m J_{|\sigma|}^{(2)} + J_{|\sigma|}^{(4)}$. Experimentally, all four contributions can be extracted by switching the sign of SAM (σ) and the OAM order (m) of the LG beam, as given by Equations (S21–S24) Note S3, Supporting Information. After integration, the current flowing along both the radial and azimuthal directions survives for the OPGE-related terms: $m \cdot \sigma J^{(1)}$ and $m J_{|\sigma|}^{(2)}$, as given by Equations (S12 and S13) in Note S3, Supporting Information. To detect radial and azimuthal currents, U-shaped, Ω-shaped, and starfish-shaped electrodes were designed, which are sensitive to radial (U-shaped) and azimuthal (Ω-shaped and starfish-shaped) currents, respectively. The different geometries of the electrodes help to identify and characterize the photoresponse from the helical phase profile of the OAM beam.

The mechanism of the OPGE can be understood as light transfers its OAM and energy simultaneously to the electrons. Because the optical phase varies in the azimuthal direction, it induces a spatial imbalance of the excited carriers, producing a net current. This is similar to the photon drag effect, which transfers linear momentum and energy from the photon to the electron.[17] However, upon normal incidence, the photon momentum along the out-of-plane direction was forbidden in our measurements. In addition, because the LG beam has an azimuthal phase profile and annular intensity profile, it can generate current from the spatially dispersive photogalvanic effect (s-PGE), which is proportional to the local light intensity gradient,[18] and is given by the term $\sigma J^{(3)} + J_{|\sigma|}^{(4)}$. Clearly, s-PGE is only sensitive to the light SAM, and $\sigma J^{(3)}$ provides the spatially dispersive circular photogalvanic effect (s-CPGE) contribution. Although part of the s-PGE is sensitive to both the light helicity and $|m|$, denoted as s-CPGE, it does not change sign when the vortex beam changes from $+|m|$ to $-|m|$ because the local light intensity is preserved when the OAM order reverses sign. In addition to these photocurrent generation mechanisms from the second-order nonlinear response, a space-charge DC electric field ($\mathbf{E}_{DC}$) assisted third-order nonlinear CPGE at the vicinity of the electrodes, denoted as E_{DC}-CPGE, can also contribute to the circular polarization dependent photocurrent, which will be discussed in the last session. Otherwise, photocurrent generated by other mechanisms cannot exhibit any SAM or OAM dependence. A detailed discussion of the other photocurrent generation mechanisms can be found in Note S4, Supporting Information.

**ADVANCED
SCIENCE NEWS**

www.advancedsciencenews.com

**ADVANCED
MATERIALS**

www.advmat.de

3. OPGE Response of TaIrTe$_4$

To perform the measurement, TaIrTe$_4$ flakes were exfoliated from the bulk material and fabricated into devices with U-shaped electrodes to collect the radial current, as shown in Figure 1b and Figure S3a, Supporting Information, or into devices with Ω-shaped and starfish-shaped electrodes to collect the azimuthal current, as shown in Figures S5a and S6a, Supporting Information. The typical thickness of TaIrTe$_4$ flakes used for device fabrication is between 100 and 200 nm, which is close to the penetration depth (≈140 nm) of TaIrTe$_4$ at 4 μm.[19] Figure 1c shows the schematic of the OPGE measurement on a U-shaped electrode device. When the OAM order of light is switched from +|m| to −|m|, the radial current from the OPGE effect switches its sign, while its amplitude should be proportional to the OAM order (m) according to Equation (S11), Supporting Information. Figure 1d–f illustrate typical scanning photocurrent microscopy (SPCM) images at 633 nm and 4 μm excitations (Figure 1e,f) of a U-shaped electrode device together with in situ scanning reflection microscopy (Figure 1d). The spatial resolutions of these excitations were ≈3 μm and 10 μm, respectively. The radii of the inner and outer electrodes were ≈12 and 20 μm, respectively, and the photocurrent responses were mainly from the region between the two electrodes, which included both the TaIrTe$_4$–metal junctions and the inner area between the metal electrodes. A systematic characterization of the TaIrTe$_4$ photodetector under the excitation of a Gaussian beam, including the responsivity, specific detectivity, and response time, was presented in our previous work.[13d] Under the excitation of a higher-order LG beam, the responsivity of the device was reduced because of the very different beam profiles. The basic photoresponse characterization results under the excitation of the LG beam with an OAM order of 4, including the responsivity and response time, are presented in Note S5, Supporting Information.

The experimental setup for examining the OPGE response to the OAM of light is shown in **Figure 2**a. The OAM beams were obtained by passing a basic mode Gaussian beam through a series of SPPs with a designed OAM order of 4 μm. SPPs convert a Gaussian beam into LG modes. The vortex beam was focused by a 40× reflection objective onto a ring with a radius of 16 μm. The center of the vortex beam was fixed at the center of the U-shaped electrode arcs, which were composed of two concentric semicircles and two parallel arms, as shown in Figure 2b. The configuration of the electrodes enables ≈180° solid angle collection of the radial current. In the measurement results presented in this section, the ring-shaped OAM beam was moved to the middle of the inner and outer electrodes. The dependence of the OPGE responses on the radius and position of the excitation beam is presented separately in the next section.

To separate the photocurrent response, which depends on the OAM of light, a quarter-wave plate (QWP) is positioned after a linear polarizer to continuously tune the polarization of the vortex beam. By rotating the QWP angle ($\hat{\theta}$) by 180°, the polarization of light undergoes linear ($\hat{\theta}=0°$)-left circular, ($\hat{\theta}=45°$)-linear ($\hat{\theta}=90°$)-right circular, and ($\hat{\theta}=135°$)-linear ($\hat{\theta}=180°$) polarization states. Figure 2c shows the photocurrent response under a constant excitation power of 2.5 mW with different OAM orders. In the measurements, the radius of the ring was kept the same for different OAM orders, as defined by the U-shaped electrodes. Benefiting from the topological enhancement of the shift current response, as reported in our previous work,[13a] the device showed an appreciable photocurrent response at 4 μm. The photocurrent response can be divided into three components with different $\hat{\theta}$-periodicities
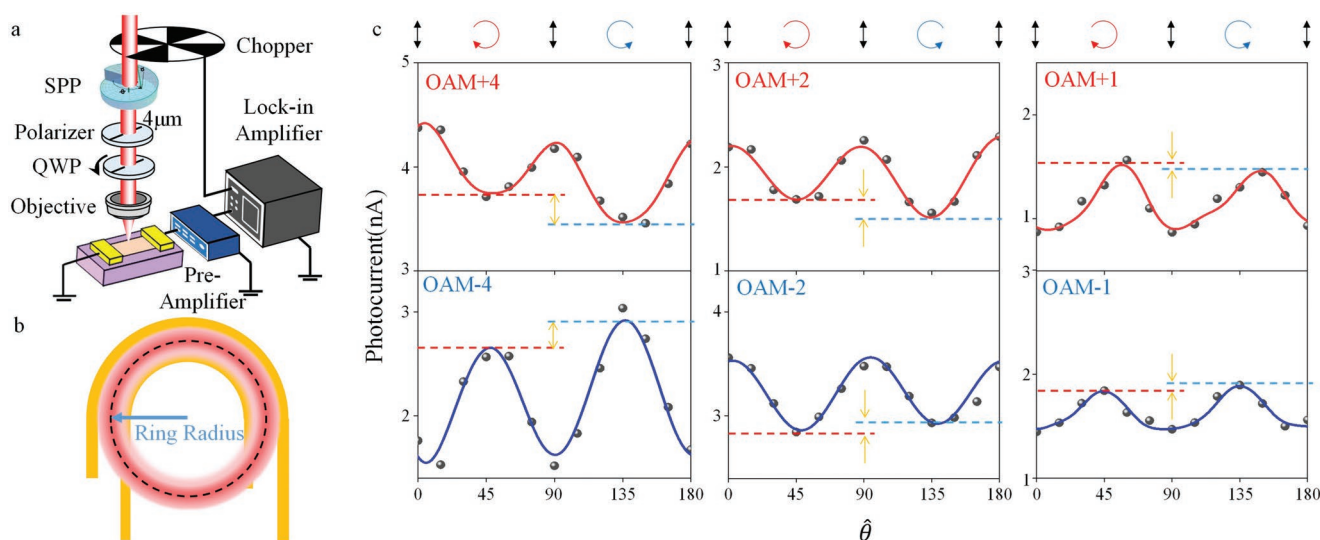

Figure 2. OPGE current measurement of TaIrTe$_4$ device with U-shaped electrodes. a) Schematic diagram of the OPGE measurement. b) Schematic diagram of a photodetector device with U-shaped electrodes. The light spot of the LG beam is focused on the center of the arcs defined by the U-shape electrodes. c) The photocurrent amplitudes measured as a function of $\hat{\theta}$, under the excitation of LG beams with OAM order from +4, +2, and +1 (red curve) to −1, −2, and −4 (blue curve). Each data point in the measurement was measured 100× and presented as the mean. The blue and red dashed lines mark the responses from the excitation of right and left circular polarization, respectively, and the differences between them correspond to the CPGE components of the photocurrent responses.

after the Fourier transform of the $\hat{\theta}$-dependent photocurrent response: a 180°-periodicity component (J_C), which accounts for the CPGE response related to different circular polarizations ($\sigma = \pm 1$); a 90°-periodicity component (J_L), which accounts for the anisotropic response to different linear polarization directions; and a constant component (J_0), which is polarization-independent. When the incident beams have positive OAMs, the photocurrent generated by the left circularly polarized excitation ($\hat{\theta} = 45°$) is stronger than that generated by the right circularly polarized excitation ($\hat{\theta} = 135°$). In contrast, when the incident beams have negative OAMs, the photocurrent generated by the left circularly polarized excitation ($\hat{\theta} = 45°$) is weaker than that generated by the right circularly polarized excitation ($\hat{\theta} = 45°$). The results show that both positive and negative OAM beams give rise to circular polarization-dependent photocurrent, and the amplitude of J_C increases monotonically with the OAM order m, while J_C has opposite signs for $+|m|$ and $-|m|$ beam excitations.

According to Equation (2), both $m \cdot \sigma J^{(1)}$ and $\sigma J^{(3)}$ can contribute to the CPGE response, but only $m \cdot \sigma J^{(1)}$ is proportional to the OAM order m, and the response should switch sign as the light polarization switches from left circular to right circular. **Figure 3**a summarizes the extracted CPGE component (J_C) as a function of the OAM order (m). J_C displays step-like changes for m ranging from −4 to +4, showing that the CPGE response is dominated by $m \cdot \sigma J^{(1)}$ and that the contribution from $\sigma J^{(3)}$ is minor. Meanwhile, we can extract the anisotropic response component (J_L) and the polarization-independent component (J_0). As shown in Figure 3b, J_C is clearly proportional to m, whereas J_L and J_0 do not show a clear m dependence, which indicates that J_L and J_0 are not responsible for the response to the OAM of light. We confirmed these results by repeating the measurement on another device with U-shaped electrodes, as shown in Figures S3 and S4, Supporting Information. Furthermore, we also fabricated devices with Ω-shaped and starfish-shaped electrodes to collect the azimuthal current, and similar step-like changes in J_C with m ranging from −4 to +4 were observed, as shown in Figures S5 and S6, Supporting Information. According to these results, the OAM

order could be clearly distinguished by the quantized plateau of the CPGE response at 4 µm.

4. Beam-Size and Spatial-Dependent OPGE Measurements

The current collection efficiency is optimized when the rings are between the inner and outer electrodes. The CPGE response is dominated by the OPGE for the measurement geometry, and mainly originates from the $m \cdot \sigma J^{(1)}$ term. This is no longer valid when the OAM beam does not match the U-shaped electrodes, that is, if the beam size increases or decreases, or if the beam center is moved off the center. In the following section, we discuss beam size and excitation position-dependent measurements that were performed on a U-shaped electrode device. Such measurements can help identify other responses that are circular polarization-dependent, and confirm that the OPGE response is along the radial direction for the U-shaped electrode geometry.

Figure 4 shows the beam size dependence of the photocurrent for five different beam radii and opposite OAM orders ($m = \pm 4$). The radii of the vortex beam are chosen as follows: smaller than the inner electrode (7.5 µm, Figure 4a)—just covering the inner electrode (12 µm, Figure 4b)—in the middle of the inner and outer electrodes (16 µm, Figure 4c)—just covering the outer electrode (20 µm, Figure 4d)—larger than the outer electrode (28 µm, Figure 4e). The sign and amplitude of J_C at different OAMs show a complex dependence on the beam radius (Figure 4f). At a radius of 16 µm, J_C has a similar amplitude, but switches sign for the opposite OAM order, which is consistent with the conclusion made in the previous section. At a radius of 12 or 20 µm, J_C does not switch sign for opposite OAM orders for radii of 12 or 20 µm. Furthermore, at a radius of 7.5 or 28 µm, J_C maintains the same sign, but the amplitude of J_C becomes much smaller.

The beam size dependence indicates that a significant CPGE still exists when the beam radii do not match the electrodes (Figure 4a,b,d,e). Such a CPGE is irrelevant to the OAM of light,
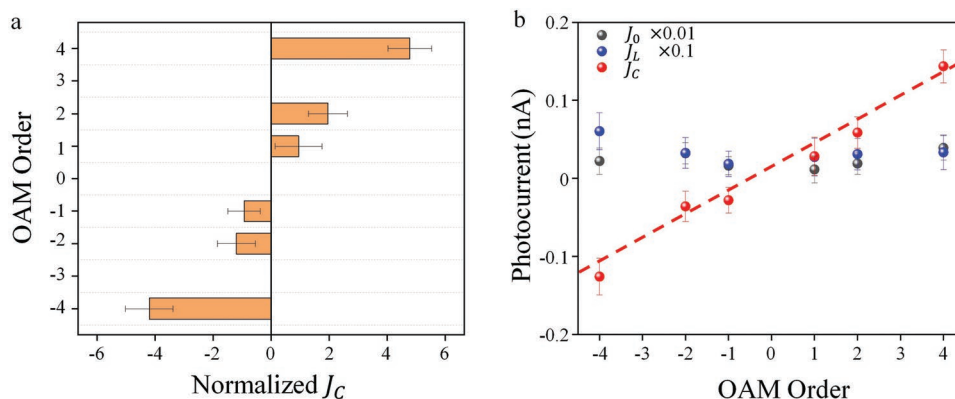

Figure 3. Evidence of the OPGE current generated by the OAM of light and its dependence on the OAM order. a) Normalized J_C under the excitation of LG beams with OAM order ranging from −4 to 4. The error bars represent the standard deviations of the fittings shown in Figure 2c. b) Three components of the measured photocurrent as a function of the OAM order: J_0, J_L, and J_C. J_0 and J_L are scaled by factors of 0.01 and 0.1, respectively, and their error bars are not scaled, to be visible in the plot.
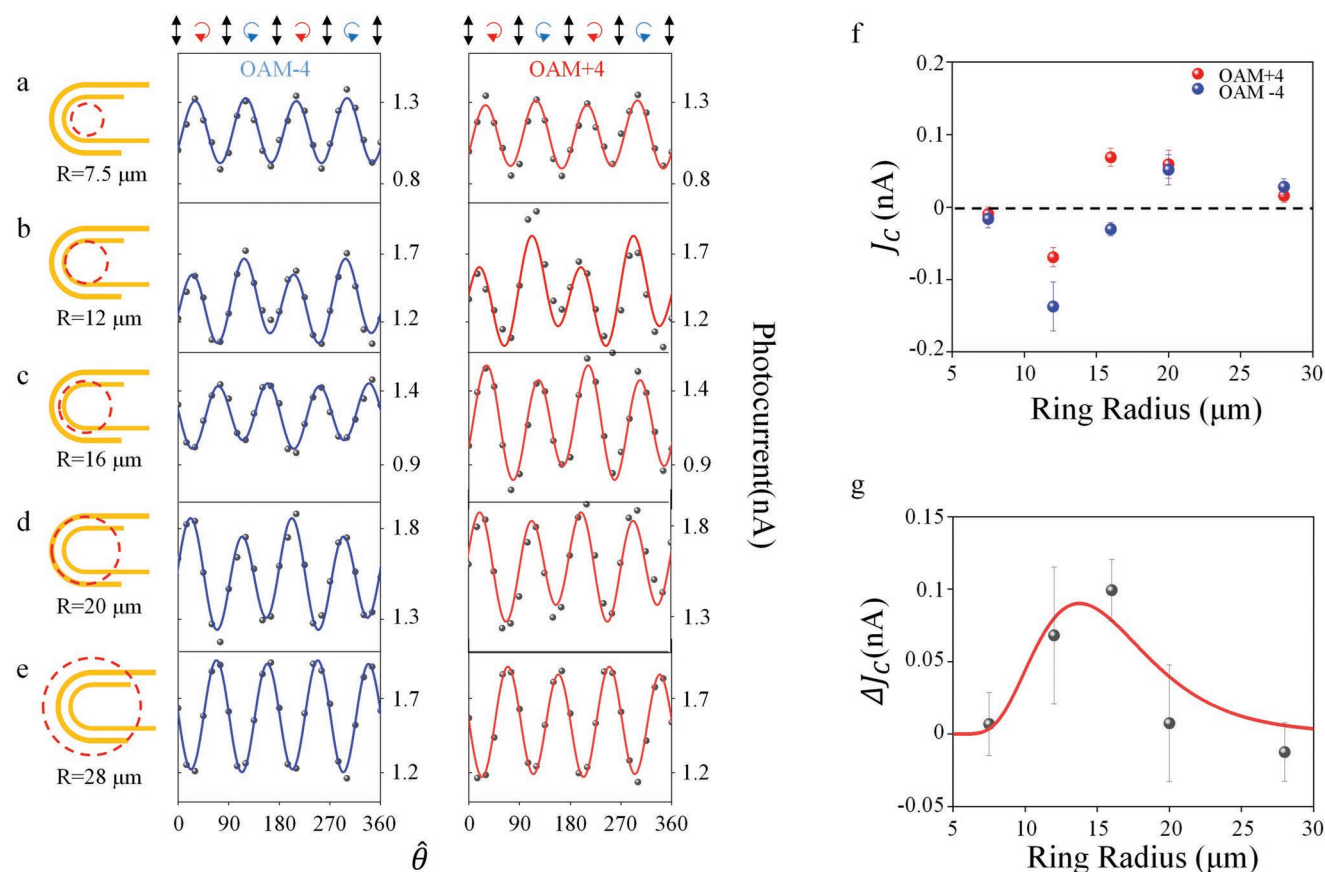
Figure 4. Spot-size-dependent measurements obtained using a U-shaped electrodes device under excitation of the LG beam with OAM order +4 and −4. a–e) Photocurrent measured for five different spot sizes. All data are plotted in the same scale. Each data point in the measurement was measured 10 times and presented as the mean. The schematic diagrams on the left of each figure show the relative position between the U-shaped electrodes and vortex beam with different spot sizes. f) The J_C component measured at five different spot sizes. Error bars represent the standard deviations of the fitting shown in (a–e). g) The $\Delta J_C = J_C(OAM + 4) - J_C(OAM - 4)$ as a function of the beam radius (black balls) and the fitting result (red curve) using $J_{OPGE} = km\int_{r_1}^{r_2} |E|^2\, dr$, where k is the fitting parameter.

and it could come from the $j_{|m|}^{(3)}(r, \phi, z)$ term, which includes the s-CPGE effect. Besides the $j_{|m|}^{(3)}(r, \phi, z)$ term, it can also result from higher-order effects, such as E_{DC}-CPGE, as reported in previous works.[13a,20] Although materials with the C_{2v} point group do not support any second-order PGE that can provide planar currents from symmetry considerations, the CPGE is allowed for the third-order nonlinear response by including an E_{DC}, which is denoted as E_{DC}-CPGE. The E_{DC} can be due to multiple effects, such as the built-in electric field generated by the work function difference between the semimetal and the metal contact or the photothermoelectric effect. In either case, the E_{DC} was limited mainly to the area near the contacts. The E_{DC} switches sign at the semimetal-contact and contact-semimetal interface; thus, the contribution from E_{DC}-CPGE switches sign. When the vortex beam is in the middle of the inner and outer electrodes, the E_{DC}-CPGE generated from the interfaces with the inner and outer electrodes has an opposite sign, and they almost cancel each other. However, as the radius increases or decreases where the ring can only cover one electrode, E_{DC}-CPGE is generated solely from the interface with one electrode. For 12 µm and 20 µm excitation radii, which cover the inner or outer electrode, respectively, the signs of E_{DC}-CPGE

should be opposite to each other. Furthermore, E_{DC}-CPGE is associated with the electric field instead of its gradient; thus, it is independent of the OAM of light and contributes equally to the response for both $+ m$ and $- m$ vortex beam excitations. The $j_{|m|}^{(3)}(r, \phi, z)$ term does not switch sign when the vortex beam switches from $+|m|$ to $-|m|$. These analyses are consistent with our measurement results.

Therefore, by plotting $\Delta J_C = J_C(OAM + 4) - J_C(OAM - 4)$ in Figure 4g, we find that the beam radius dependence of ΔJ_C is similar to that observed for WTe_2 (Figure S9, Supporting Information of Ref. [11]). This dependence can be understood by analyzing the OPGE in these measurement configurations. The current from the OPGE can be estimated from $J_{OPGE} \propto \int_0^\theta \int_{r_1}^{r_2} j_r(\phi) r\, dr\, d\phi \propto m\int_{r_1}^{r_2} |E|^2\, dr$, where $j_r(\phi) \propto m\frac{1}{r}|E|^2$ is the local OPGE current generated by the vortex beam at the position (r, φ) between the electrodes. For each LG mode, the geometrical factor was determined by the electrode geometry and beam parameters. Qualitatively, when the radius of the vortex beam is either smaller than the inner electrode (≈ 7.5 µm) or larger than the outer electrode (≈ 28 µm), the integrand is zero between the two electrodes, which implies that the OPGE
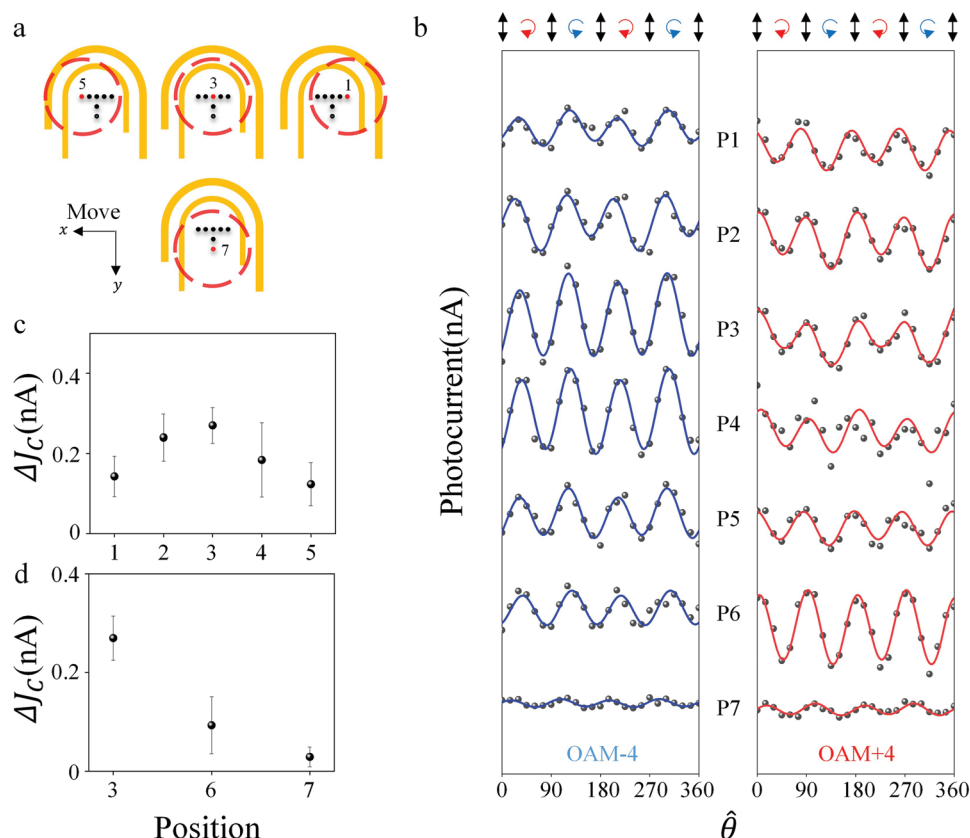
Figure 5. Excitation-position-dependent OPGE measurements obtained using a U-shaped electrodes device. a) Schematic of the beam on a U-shaped electrodes device, the beam center locations are marked by the red dots, and the beam profiles are marked by the red dash circles. The OPGE values are measured when the beam spot is moved along both the x and y directions. b) Photocurrent data measured at seven positions, from P1–P7, with $m = \pm 4$. Each data point in the measurement was measured 30× and presented as the mean. c) The OPGE current magnitude measured at five different positions along the x direction. d) The OPGE current magnitude measured at three positions along the y direction. $\Delta J_C = J_C (OAM + 4) - J_C(OAM - 4)$; the error bars represent the standard deviations of the fittings shown in (b).

current vanishes. Otherwise, when any part of the ring of the vortex beam is located between these two U-shaped electrodes, the OPGE current becomes nonzero, with a value proportional to $\int_{r_1}^{r_2} |E|^2 \, dr$ discussed above. In particular, as the radius of the vortex beam is located in the middle of the U-shaped electrodes (≈ 16 μm), the collected OPGE current was optimized. The experimental data were well fitted by the function $km\int_{r_1}^{r_2} |E|^2 \, dr$ with a single fitting parameter k.

Next, we focus on the spatial dependence of the OPGE current with a fixed beam radius (≈ 16 μm), as shown in **Figure 5**. The OPGE current reached its maximum when the beam center was at the center of the arcs (at position P3). As the beam center moves away from the center along the x direction (either to the left or to the right), or as it moves down along the y direction, the magnitude of the OPGE current gradually decreases, as shown in Figures 5c and 5d. This is because the U-shaped electrodes provide a good limit on the photocurrent flow, and the magnitude of the collected OPGE is proportional to the solid angle formed by the beam center and the electrodes. The solid angle decreases regardless of the direction in which the beam moves off the center of the electrodes, and thus the OPGE response also decreases. The spatially dependent results

are consistent with the fact that the generated OPGE current flows along the radial direction instead of the directions determined by the crystallographic axes. Together, the beam size and spatially dependent measurements further confirm that the OPGE current is collected effectively by the U-shaped electrodes when the beam size and position match the electrode structure.

5. Summary and Prospective

Our results demonstrate that photodetectors based on the type-II Weyl semimetal TaIrTe$_4$ with specially designed electrode structures can directly resolve the topological charge of the OAM of light in the mid-infrared wavelength range. The topological charge of a scalar OAM beam can be resolved using the photocurrent plateau driven by the OPGE response. Combined with previous experimental demonstrations that exhibit that TaIrTe$_4$ is sensitive to both the direction of linearly polarized light owing to its anisotropic photocurrent response[13d,21] and the helicity of light owing to the chiral nature of the Weyl cone as a Weyl semimetal,[22] TaIrTe$_4$ represents a class of topological semimetals that is suitable for both OAM and polarization-sensitive photodetection in the mid-infrared

waveband. A mixture of a variety of OAM orders and the polarization of light may be resolved simultaneously by using a small matrix of well-designed electrodes. Once the device geometry is fixed, characterized, and calibrated, a single device matrix can resolve the full optical parameters of light by back-end processing of the measured photocurrent signals from the different matrix components. Considering that the improvement of the absolute detectivity is very challenging for mid-infrared photodetectors without cooling, it is crucial that the image resolution and intricate target recognition capability of a focal plane array can be promoted by polarization[23] and OAM sensitivity, as discovered in this work. We expect the results of this work to further advance mid-infrared photodetection based on topological semimetals as a disruptive technology alternative to the conventional roadmap.[14a]

6. Experimental Section

Material Growth and Device Fabrication: All of the elements used in the sample growth were stored and acquired in an argon-filled glovebox. $TaIrTe_4$ single crystals were synthesized by a solid-state reaction using a Te flux. Single crystals were grown using the method described in ref. [13]. $TaIrTe_4$ flakes were mechanically exfoliated from bulk $TaIrTe_4$ crystals and transferred onto 300 nm SiO_2/Si substrates. A standard electron-beam lithography technique was used to pattern electrodes with designed shapes. Electrodes consisting of 10 nm Cr and 300 nm Au were deposited using an electron-beam evaporator.

Optical Characterizations: Standard SPCMs were performed under ambient conditions using a 632.8 nm He–Ne laser and a CW quantum cascade laser source emitting at 4 μm. The laser beam was focused by a 40× transmissive objective lens (632.8 nm) and a 40× reflection objective (4 μm). A scanning mirror or motorized stage was used to scan the light beam over the device. The reflection signal and photocurrent were recorded simultaneously to obtain reflection and photocurrent responses.

For the OPGE measurement, the vortex beams carrying different OAM were generated by a series of spiral phase plates designed and manufactured for a 4 μm laser. Either ZnSe or silicon was used to manufacture the spiral phase plates to obtain the best transmittance at 4 μm with an OAM order of up to 4. A motorized rotation stage was used to rotate the quarter-wave plate to tune the polarization of the vortex beam. The waveplate was calibrated to rule out experimental artifacts in the CPGE component, which may affect the validity of this work (Note S9, Supporting Information). The vortex beam was focused by a 40× reflection objective, and the spot sizes of the vortex beam could be adjusted by varying the distance between the objective and the devices.

In both the scanning photocurrent and OPGE measurements, the laser beam was modulated using a mechanical chopper (≈373 Hz), and the short-circuit photocurrent signal was first amplified to a voltage signal by a current pre-amplifier. Then, the voltage output from the pre-amplifier was measured by a lock-in amplifier.

Statistical Analysis: The SPCM images were drawn using MATLAB (R2021b). Data from the OPGE measurements were analyzed and pre-processed using Origin Pro (2020b), including fast Fourier transform and curve-fitting programs. Each data point in the OPGE measurements ranged from 10–100×. The J_C data were fitted and presented as the mean± standard deviation.

Supporting Information

Supporting Information is available from the Wiley Online Library or from the author.

Conflict of Interest

The authors declare no conflict of interest.

Author Contributions

D.S. conceived of the study and designed the experiments. P.Y. and Z.L. provided bulk TaIrTe4 materials. J.W.L. fabricated the device and performed the measurements with the help of J.C.M., Z.P.F., and X.M.S under the supervision of D.S. P.Z. contributed to vertex beam generation used in the experiment. Y.S. contributed to the application of OAM-sensitive detection. J.L.C contributed to the theoretical analysis. J.W.L. and D.S. analyzed the experimental results. J.W.L. and D.S. wrote the manuscript, assisted by J.L.C., Y.S., and P.Z. All authors commented on the manuscript.

Data Availability Statement

The data that support the findings of this study are available from the corresponding author upon reasonable request.

[1] P. Coullet, L. Gil, F. Rocca, *Opt. Commun.* **1989**, *73*, 403.

[2] a) A. Ashkin, *Phys. Rev. Lett.* **1970**, *24*, 156; b) H. He, M. E. J. Friese, N. R. Heckenberg, H. Rubinsztein-Dunlop, *Phys. Rev. Lett.* **1995**, *75*, 826.

[3] a) Y. Jin, O. J. Allegre, W. Perrie, K. Abrams, J. Ouyang, E. Fearon, S. P. Edwardson, G. Dearden, *Opt. Express* **2013**, *21*, 25333; b) O. J. Allegre, Y. Jin, W. Perrie, J. Ouyang, E. Fearon, S. P. Edwardson, G. Dearden, *Opt. Express* **2013**, *21*, 21198.

[4] a) S. Fürhapter, A. Jesacher, S. Bernet, M. Ritsch-Marte, *Opt. Express* **2005**, *13*, 689; b) F. Tamburini, G. Anzolin, G. Umbriaco, A. Bianchini, C. Barbieri, *Phys. Rev. Lett.* **2006**, *97*, 163903.

[5] a) G. Molina-Terriza, J. P. Torres, L. Torner, *Nat. Phys.* **2007**, *3*, 305; b) M. Erhard, R. Fickler, M. Krenn, A. Zeilinger, *Light: Sci Appl* **2018**, *7*, 17146.

[6] a) J. A. Anguita, J. Herreros, I. B. Djordjevic, *IEEE Photonics J.* **2014**, *6*, 7900811; b) J. T. Barreiro, T.-C. Wei, P. G. Kwiat, *Nat. Phy.* **2008**, *4*, 282.

**ADVANCED
SCIENCE NEWS**

www.advancedsciencenews.com

**ADVANCED
MATERIALS**

www.advmat.de

[7] a) M. Harwit, *Astrophys. J.* **2003**, *597*, 1266; b) G. Foo, D. M. Palacios, G. A. Swartzlander, *Opt. Lett.* **2005**, *30*, 3308.

[8] a) L. Allen, M. W. Beijersbergen, R. J. C. Spreeuw, J. P. Woerdman, *Phys. Rev. A* **1992**, *45*, 8185; b) A. Mair, A. Vaziri, G. Weihs, A. Zeilinger, *Nature* **2001**, *412*, 313; c) Y. Shen, X. Wang, Z. Xie, C. Min, X. Fu, Q. Liu, M. Gong, X. Yuan, *Light: Sci. Appl.* **2019**, *8*, 90.

[9] a) Z. Jin, D. Janoschka, J. Deng, L. Ge, P. Dreher, B. Frank, G. Hu, J. Ni, Y. Yang, J. Li, C. Yu, D. Lei, G. Li, S. Xiao, S. Mei, H. Giessen, F. M. zu Heringdorf, C.-W. Qiu, *eLight* **2021**, *1*, 5; b) J. Ni, C. Huang, L.-M. Zhou, M. Gu, Q. Song, Y. Kivshar, C.-W. Qiu, *Science* **2021**, *374*, eabj0039; c) P. Miao, Z. Zhang, J. Sun, W. Walasik, S. Longhi, M. Litchinitser Natalia, L. Feng, *Science* **2016**, *353*, 464; d) Z. Xie, T. Lei, F. Li, H. Qiu, Z. Zhang, H. Wang, C. Min, L. Du, Z. Li, X. Yuan, *Light: Sci. Appl.* **2018**, *7*, 18001; e) T. Stav, A. Faerman, E. Maguid, D. Oren, V. Kleiner, E. Hasman, M. Segev, *Science* **2018**, *361*, 1101; f) Z. Zhang, X. Qiao, B. Midya, K. Liu, J. Sun, T. Wu, W. Liu, R. Agarwal, M. J. Josep, S. Longhi, M. Litchinitser Natalia, L. Feng, *Science* **2020**, *368*, 760; g) B. Chen, Y. Wei, T. Zhao, S. Liu, R. Su, B. Yao, Y. Yu, J. Liu, X. Wang, *Nat. Nanotechnol.* **2021**, *16*, 302.

[10] a) A. M. Yao, M. J. Padgett, *Adv. Opt. Photonics* **2011**, *3*, 161; b) L. E. E. de Araujo, M. E. Anderson, *Opt. Lett.* **2011**, *36*, 787; c) A. Mourka, J. Baumgartl, C. Shanor, K. Dholakia, E. M. Wright, *Opt. Express* **2011**, *19*, 5760; d) H.-L. Zhou, D.-Z. Fu, J.-J. Dong, P. Zhang, D.-X. Chen, X.-L. Cai, F.-L. Li, X.-L. Zhang, *Light: Sci. Appl.* **2017**, *6*, e16251; e) J. Zhu, P. Zhang, F. Wang, Y. Wang, Q. Li, R. Liu, J. Wang, H. Gao, F. Li, *Opt. Express* **2021**, *29*, 5419.

[11] Z. Ji, W. Liu, S. Krylyuk, X. Fan, Z. Zhang, A. Pan, L. Feng, A. Davydov, R. Agarwal, *Science* **2020**, *368*, 763.

[12] N. B. Clayburn, J. L. McCarter, J. M. Dreiling, M. Poelker, D. M. Ryan, T. J. Gay, *Phys. Rev. B* **2013**, *87*, 035204.

[13] a) J. Ma, Q. Gu, Y. Liu, J. Lai, P. Yu, X. Zhuo, Z. Liu, J.-H. Chen, J. Feng, D. Sun, *Nat. Mater.* **2019**, *18*, 476; b) Q. Wang, J. Zheng, Y. He, J. Cao, X. Liu, M. Wang, J. Ma, J. Lai, H. Lu, S. Jia, D. Yan, Y. Shi, J. Duan, J. Han, W. Xiao, J.-H. Chen, K. Sun, Y. Yao, D. Sun, *Nat. Commun.* **2019**, *10*, 5736; c) J. Lai, X. Liu, J. Ma, Q. Wang, K. Zhang, X. Ren, Y. Liu, Q. Gu, X. Zhuo, W. Lu, Y. Wu, Y. Li, J. Feng, S. Zhou, J. H. Chen, D. Sun, *Adv. Mat.* **2018**, *30*, 1707152; d) J. Lai, Y. Liu, J. Ma, X. Zhuo, Y. Peng, W. Lu, Z. Liu, J. Chen, D. Sun, *ACS Nano* **2018**, *12*, 4055; e) Q. Wang, C. Z. Li, S. Ge, J. G. Li, W. Lu, J. Lai, X. Liu, J. Ma, D. P. Yu, Z. M. Liao, D. Sun, *Nano Lett.* **2017**, *17*, 834; f) J. Lai, J. Ma, Y. Liu, K. Zhang, X. Zhuo, J. Chen, S. Zhou, D. Sun, *2D Mater.* **2020**, *7*, 034003; g) G. B. Osterhoudt, L. K. Diebel, M. J. Gray, X. Yang, J. Stanco, X. Huang, B. Shen, N. Ni, P. J. W. Moll, Y. Ran, K. S. Burch, *Nat. Mater.* **2019**, *18*, 471; h) S. Chi, Z. Li, Y. Xie, Y. Zhao, Z. Wang, L. Li, H. Yu, G. Wang, H. Weng, H. Zhang, J. Wang, *Adv. Mater.* **2018**, *30*, 1801372; i) S. Kai, S. Shuai-Shuai, W. Lin-Lin, G. Cong, T. Huan-Fang, C. Gen-Fu, Y. Huai-Xin, L. Jian-Qi, *Chin. Phys. Lett.* **2017**, *34*, 117203; j) W. Zhou, J. Chen, H. Gao, T. Hu, S. Ruan, A. Stroppa, W. Ren, *Adv. Mater.* **2018**, *0*, 1804629; k) M. Yang, J. Wang, J. Han, J. Ling, C. Ji, X. Kong, X. Liu, Z. Huang, J. Gou, Z. Liu, F. Xiu, Y. Jiang, *ACS Photonics* **2018**, *5*, 3438.

[14] a) J. Liu, F. Xia, D. Xiao, F. J. Garcia de Abajo, D. Sun, *Nat. Mater.* **2020**, *19*, 830; b) T. Morimoto, N. Nagaosa, *Sci. Adv. 2*, e1501524.

[15] a) E. Haubold, K. Koepernik, D. Efremov, S. Khim, A. Fedorov, Y. Kushnirenko, S. van den Brink, S. Wurmehl, B. Buchner, T. K. Kim, M. Hoesch, K. Sumida, K. Taguchi, T. Yoshikawa, A. Kimura, T. Okuda, S. V. Borisenko, *Phys. Rev. B* **2017**, *95*, 241108; b) K. Koepernik, D. Kasinathan, D. V. Efremov, S. Khim, S. Borisenko, B. Buchner, J. van den Brink, *Phys. Rev. B* **2016**, *93*, 201101; c) I. Belopolski, S.-Y. Xu, Y. Ishida, X. Pan, P. Yu, D. S. Sanchez, H. Zheng, M. Neupane, N. Alidoust, G. Chang, T.-R. Chang, Y. Wu, G. Bian, S.-M. Huang, C.-C. Lee, D. Mou, L. Huang, Y. Song, B. Wang, G. Wang, Y.-W. Yeh, N. Yao, J. E. Rault, P. Le Fèvre, F. Bertran, H.-T. Jeng, T. Kondo, A. Kaminski, H. Lin, Z. Liu, *Phys. Rev. B* **2016**, *94*, 085127.

[16] R. L. Phillips, L. C. Andrews, *Appl. Opt.* **1983**, *22*, 643.

[17] J. L. Cheng, N. Vermeulen, J. E. Sipe, *Sci. Rep.* **2017**, *7*, 43843.

[18] Z. Ji, G. Liu, Z. Addison, W. Liu, P. Yu, H. Gao, Z. Liu, A. M. Rappe, C. L. Kane, E. J. Mele, R. Agarwal, *Nat. Mater.* **2019**, *18*, 955.

[19] F. Le Mardelé, D. Santos-Cottin, E. Martino, K. Semeniuk, S. B. David, F. Orbanić, M. Novak, Z. Rukelj, C. C. Homes, A. Akrap, *Phys. Rev. B* **2020**, *102*, 045201.

[20] a) J. Ma, R. A. Muniz, S. Qi, J. Lai, K. Zhang, Y. Liu, X. Zhuo, S. Chen, J.-H. Chen, S. Zhou, D. Sun, *2D Mater.* **2021**, *8*, 025016; b) A. Rasmita, C. Jiang, H. Ma, Z. Ji, R. Agarwal, W.-b. Gao, *Optica* **2020**, *7*, 1204; c) S. Dhara, J. M. Eugene, R. Agarwal, *Science* **2015**, *349*, 726.

[21] X. Zhuo, J. Lai, P. Yu, Z. Yu, J. Ma, W. Lu, M. Liu, Z. Liu, D. Sun, *Light: Sci. Appl.* **2021**, *10*, 101.

[22] Q. Ma, S.-Y. Xu, C.-K. Chan, C.-L. Zhang, G. Chang, Y. Lin, W. Xie, T. Palacios, H. Lin, S. Jia, P. A. Lee, P. Jarillo-Herrero, N. Gedik, *Nat. Phys.* **2017**, *13*, 842.

[23] a) S. G. Demos, R. R. Alfano, *Appl. Opt.* **1997**, *36*, 150; b) J. E. Solomon, *Appl. Opt.* **1981**, *20*, 1537; c) Y. W. Zhou, Z. F. Li, J. Zhou, N. Li, X. H. Zhou, P. P. Chen, Y. L. Zheng, X. S. Chen, W. Lu, *Sci. Rep.* **2018**, *8*, 15070.